



The high-temperature corrosion of Hastelloy N alloy (UNS N10003) in molten fluoride salts analysed by STXM, XAS, XRD, SEM, EPMA, TEM/EDS



Xiang-Xi Ye^a, Hua Ai^{a,b}, Zhi Guo^c, Hefei Huang^a, Li Jiang^{a,b}, Jianqiang Wang^{a,*},
Zhijun Li^{a,*}, Xingtai Zhou^a

^a Center for Thorium Molten Salts Reactor System, Shanghai Institute of Applied Physics, Chinese Academy of Sciences, Shanghai 201800, PR China

^b University of Chinese Academy of Sciences, Beijing 100049, PR China

^c Shanghai Synchrotron Radiation Facility, Shanghai Institute of Applied Physics, Chinese Academy of Sciences, Shanghai 201800, PR China

ARTICLE INFO

Article history:

Received 8 November 2015

Received in revised form 7 January 2016

Accepted 5 February 2016

Available online 8 February 2016

Keywords:

A. Nickel

A. Superalloys

B. AFS

B. EPMA

C. Alkaline corrosion

C. High temperature corrosion

ABSTRACT

The effect of Fe ion impurity on the corrosion behavior of Hastelloy N (UNS N10003) alloy in molten FLi-NaK salts at 850 °C has been investigated by combined synchrotron radiation and other characterization techniques. Results showed that Mo and Cr were depleted from the alloy surface, where Fe-rich layer formed. The corrosion process was mainly controlled by the redox reaction between Fe ion and Cr, and no new compound with high valence state formed in the alloy surface. The loss of Mo and Cr in M₁₂C carbide occurred due to the presence of a concentration-gradient between M₁₂C carbide and matrix.

© 2016 Elsevier Ltd. All rights reserved.

1. Introduction

Interests in use of molten fluoride salts are increasing for various applications such as thermal storage, electrolyte, coolant or fuel in a molten salt reactor (MSR) [1–3], but corrosion of structural materials in molten fluorides still poses a radical challenge for the application of molten fluorides [4–6]. Unlike high temperature applications of alloys in oxygen-containing environments, in which the formation of self-healing protective surface oxide films such as Cr₂O₃ and Al₂O₃ can reduce the rate of further oxidation, in fluoride salts systems, the products of corrosion, metallic fluorides, are unstable in the salt. Accordingly, passivation is precluded and corrosion depends directly on the thermodynamically driven dissolution of alloy elements whose free Gibbs energies of fluoride formation are more negative [5,7]. The tendency for common alloying elements to form fluorides increases in the following order: W, Mo, Ni, Fe, Cr, Al, Na [7]. Therefore, nickel-base alloys

with low Cr and no Al are considered as structural materials for molten salt systems, among which Hastelloy N (UNS N10003) alloy, originally designed for only successfully operated experimental molten salt reactor (MSRE) by ORNL, is well proven to be promising candidate for long-term applications [5,8]. In fact, from the thermodynamic opinion, any corrosion of elements in Hastelloy N alloy could be minimal in pure molten fluoride salts because the main components of the salt (LiF, BeF₂, NaF, KF) are more stable than any potential corrosion product. Nevertheless, the general corrosion of Hastelloy N alloy was still estimated to be with a global metal loss about 5 μm per year in MSRE [9]. Several studies have demonstrated that the corrosion behavior of the alloys is significantly affected by the presence of oxidizing impurities such as H₂O, HF, and polyvalent metallic ions (Ni²⁺, Fe²⁺) in molten fluoride salts [9–12]. Moreover, oxidizing impurities can also aggravate other corrosion processes such as mass transfer driven by thermal gradient [13,14] and galvanic corrosion caused by materials with differing electromotive potentials [7,15]. Ouyang et al. [10] demonstrated that FLiNaK salts with higher H₂O content would increase intergranular corrosion and pitting of Hastelloy N alloy at 600 °C and 700 °C in molten FLiNaK salts. The good explanation for this is that H₂O can react with the fluoride ions to generate HF that

* Corresponding authors at: 2019 Jia Luo Road, Jiading District, Shanghai Institute of Applied Physics, Chinese Academy of Sciences, Shanghai 201800, PR China.

E-mail addresses: wangjianqiang@sinap.ac.cn (J. Wang), [\(Z. Li\).](mailto:lizhijun@sinap.ac.cn)

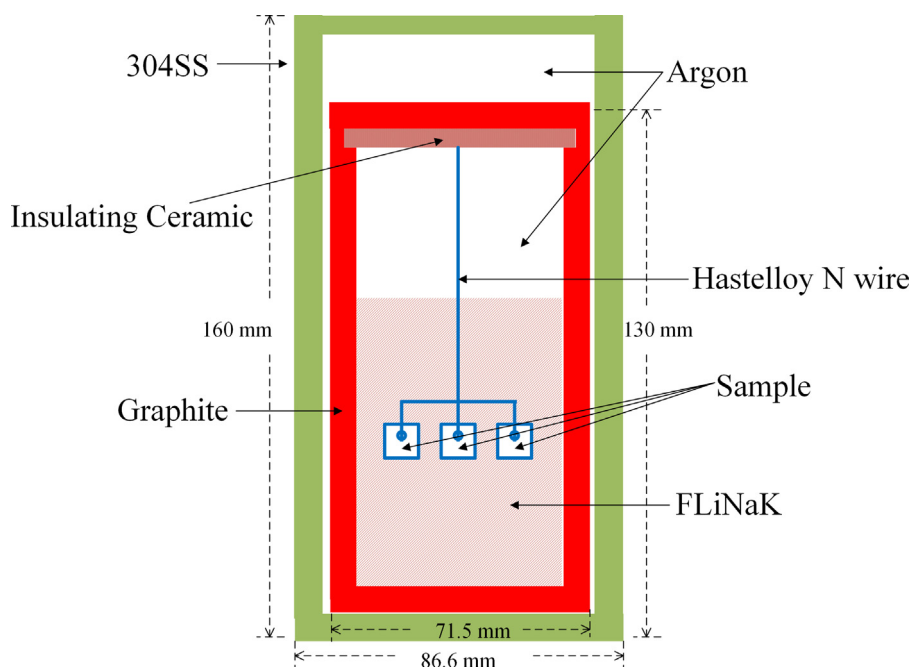


Fig. 1. Schematic diagram of experimental setup.

Table 1

Compositions of Hastelloy N alloy (wt.%), examined by inductively coupled plasma atomic emission spectrometry.

	Ni	Cr	Mo	Fe	Mn	Al	W	Si	C
Hastelloy N	Bal.	7.01	16.80	4.16	0.52	0.28	0.20	0.36	0.06

Table 2

Compositions of FLiNaK salt before and after corrosion (unit: ppm by weight, mg/kg). Each composition value is averaged over six data, expressed in terms of a mean and standard deviation.

Molten salts	Fe	Ni	Cr	Mn	Mo
FLiNaK (46.5LiF-11.5NaF-42KF mol.%, H ₂ -HF purified)	149.5 ± 7.5	60.8 ± 10.4	26.3 ± 0.6	12.9 ± 0.4	21.4 ± 3.0
FLiNaK after corrosion	29.7 ± 7.5	91.5 ± 11.6	37.5 ± 1.3	6.4 ± 0.1	32.5 ± 4.6

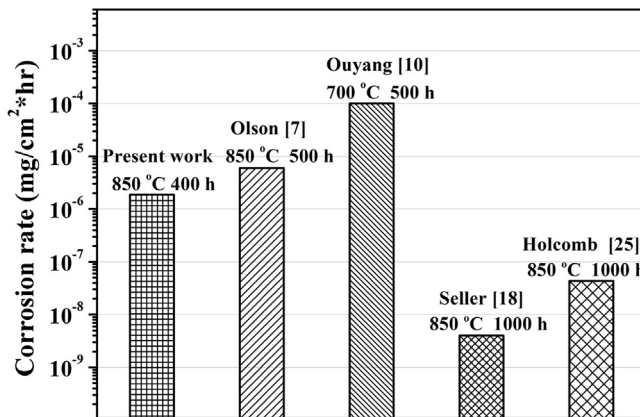


Fig. 2. Average corrosion rates of Hastelloy N alloys in FLiNaK salts at different condition [7,10,18,25]. They are calculated according to net weight loss divided by the immersion time.

will attack most elements of the alloys to form metal fluorides. Kondo et al. investigated the corrosion characteristics of some Ni-based alloys [11] and JLF-1 ferritic steel [12] under molten FLiBe salts and pointed out that HF can accelerate the corrosion rate of alloys, leading to changes in corrosion mechanism. Since H₂O and HF are among the most deleterious contaminants in fluorides, sev-

eral physical and chemical methods have been applied to purify the fluoride salts and the H₂O content could be reduced to less than 10 ppm [2,16,17]. However, in contrast with the breadth of studies about the effect of H₂O in fluoride salts on alloys, our knowledge about the corrosion effect of metallic ion impurity is still limited. Since metallic ions will also become the main source for the corrosion when the content of H₂O is controlled, understanding how metallic ions affect the corrosion in the molten fluoride salts for Ni-based alloys is crucial.

In addition, for applications like a reactor-to-hydrogen-production-plant heat transfer system, the temperature of the hot side is expected to 850 °C [2]. The performance of Hastelloy N alloy in fluoride salts at such high temperature gained increasing attentions, requiring more characteristics. Olson et al. [7] investigated the corrosion characteristics on several Ni-base alloys including Hastelloy N alloy at 850 °C in FLiNaK salts and pointed out impurities can dramatically influence corrosion. Sellers et al. [18] compared the performance of Hastelloy N alloy and 316L stainless steels in the similar condition, although the emphasis was put on the galvanic corrosion caused by interaction with graphite.

With above ideas in mind, in the present work, corrosion tests of Hastelloy N (UNS N10003) alloys, were performed in molten fluoride salts at 850 °C. FLiNaK salts (LiF-NaF-KF: 46.5–11.5–42 mol.%) with relatively high content of Fe impurities were selected for this study to investigate the effect of the metallic ion impurity on the corrosion behavior. Additionally, FLiNaK salts has also been con-

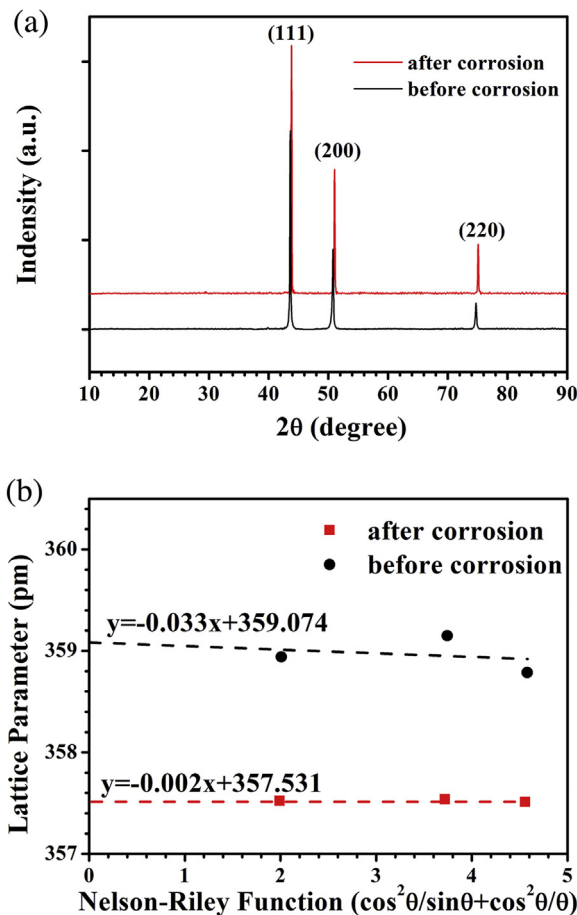


Fig. 3. (a) XRD patterns of Hastelloy N alloys before (black) and after corrosion (red) test in molten FLiNaK salts at 850 °C for 400 h. (b) The fitting plots of lattice parameter vs. Nelson-Riley function ($\cos^2\theta/\sin\theta + \cos^2\theta/\theta$). (For interpretation of the references to color in this figure legend, the reader is referred to the web version of this article.)

sidered as leading candidate for use as a secondary heat transfer fluid for molten salt reactor. To characterize the corrosion performance, several analytical methods, such as X-ray diffraction (XRD), scanning electron microscope (SEM), electro-Probe micro-analyzer (EPMA), transmission electron microscopy equipped with energy dispersive spectrometer (TEM/EDS) and synchrotron radiation scanning transmission X-ray microscopy (SR-STXM), were applied in a combined way to analyze the microstructure of Hastelloy N alloy after corrosion in molten FLiNaK salts, particularly on the chemistry change and chemical state of the alloy after corrosion. It is of note that, to the authors' best knowledge, SR-STXM method has not yet been applied to the Ni-base alloys to date.

2. Experimental method

Hastelloy N (UNS N10003) alloy was selected as the target material for corrosion tests. Its compositions are listed in Table 1. Three specimens with sizes of 15 mm × 10 mm × 2 mm were cut from the bulk Hastelloy N alloy. The specimens were grinded down to 1200 grit with SiC paper and polished with 0.05 μm Al₂O₃ powder. All the specimens were then ultrasonically cleaned in deionized water and alcohol, respectively.

The compositions of the FLiNaK salts (LiF-NaF-KF: 46.5–11.5–42 mol%) selected for this research are listed in Table 2. It was purified by sparging with argon H₂/HF followed by a H₂ gas mixture to remove residual water and oxygen from the molten salts (H₂O content < 10 ppm). The unit ppm mentioned

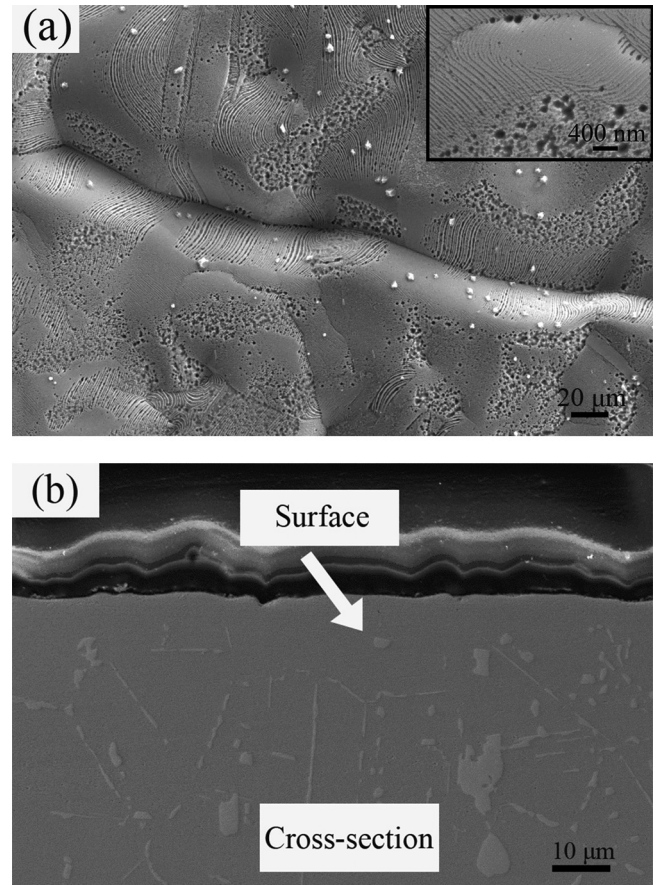


Fig. 4. Scanning electron microscopy images of Hastelloy N alloy after corrosion testing in molten FLiNaK salts at 850 °C for 400 h. (a) Surface (b) cross section.

in the present work refers to ppm by weight, mg/kg. Inductively Coupled Plasma-Optical Emission Spectroscopy (ICP-OES) analysis performed on some samples of the FLiNaK salts prior to testing showed good composition homogeneity, and the main impurities are 149.5 ppm Fe, 60.8 ppm Ni, 26.3 ppm Cr.

The schematic diagram of experimental apparatus is shown in Fig. 1. High-purity graphite crucibles were selected as the containers for corrosion tests due to the little interaction between graphite and molten fluoride salts and the presence of graphite showing no significant effect on the corrosion of Hastelloy N alloy [18]. To further minimize the galvanic corrosion, the wire fixing the specimen, made of Hastelloy N, was insulated from graphite crucible by a piece of insulating ceramic. Stainless steel shield covers with lids were chosen to reduce oxidation of the graphite crucibles at high temperature during corrosion tests. All the experimental setup was operated in a glove box filling with argon. The specimens were immersed into the FLiNaK salts with amount of about 250 g and corroded at 850 °C for 400 h. Corrosion in this length of immersion time was assumed to be primarily driven by the impurity in the FLiNaK salts [19]. The specimens after corrosion were cleaned by 1 mol/L Al(NO₃)₃ solution and deionized water. Microstructures of the alloy surface after corrosion were examined on a field emission SEM (LEO 1530VP). The crystal phases of the alloys before and after corrosion were measured on a Bruker D8 Advance XRD with a Cu Kα1 radiation source ($\lambda = 1.5406 \text{ \AA}$) conditioned by two 2.5° soller slits and a 0.025 mm Ni mask. The reflected X-ray intensity was collected by a LynxEye XE counter, using a continuous θ -2 θ scans mode at a tube power of 40 kV/40 mA in a range of 10–90° (2 θ) with step = 0.02° (2 θ) and 0.15 s per step. The elemental distribution of the corroded specimen was scanned by EPMA (Shimadzu EPMA-

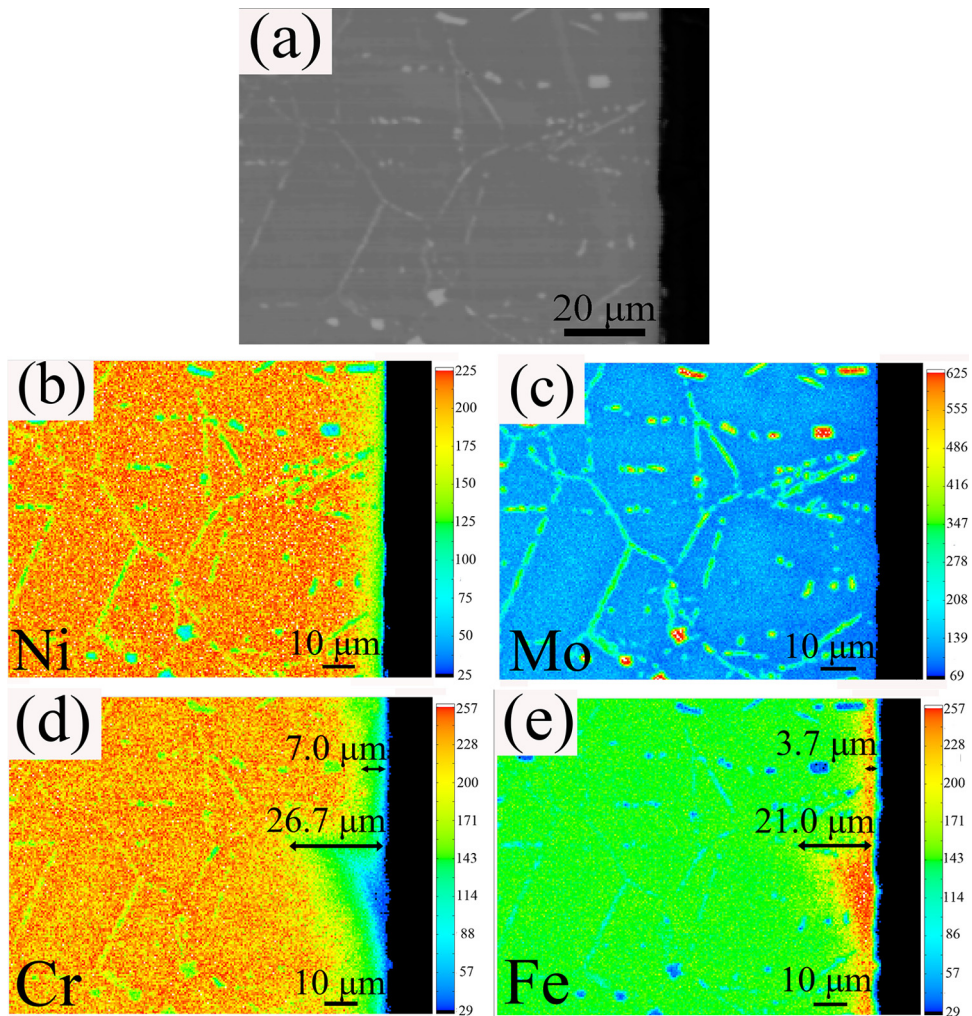


Fig. 5. Cross-sectional SEM images (a) and EPMA mappings of Hastelloy N alloy after corrosion testing in molten FLiNaK salts at 850 °C for 400 h, showing the elemental distribution of Ni (b), Mo (c), Cr (d) and Fe (e).

1720). Finally, cross-sectional sheets with thickness of about 80 nm were cut from both specimens before and after corrosion by a focus ion beam (FIB) machine (FEI Helios 600), to determine the distribution and speciation change of the elements in the specimens using a Tecnai G2 F20 TEM/EDS and SR-STXM.

SR-STXM is a powerful synchrotron-based technique to map the chemical composition and identify atoms clusters or precipitates formed in materials with high spatial resolution of about 30 nm, becoming widely applied in materials science [20–23]. In this work, the distribution and speciation of the elements in the specimens were investigated using the newly constructed BL08U1A STXM beamline at the Shanghai Synchrotron Radiation Facility (SSRF), a 3.5 GeV third-generation synchrotron source. The detailed principle of STXM and the design of the microscope have been described elsewhere [24]. The monochromatic X-ray beam was focused using a Fresnel zone plate to a 30 nm spot on the specimens. The specimens were raster scanned with synchronized detection of transmitted X-rays to generate the images. The sample was imaged in transmission mode in ultrahigh vacuum (10^{-6} Torr). A 800 lines mm^{-1} grating and 50 μm exit slit were used for Cr and Fe L-edge imaging and spectroscopy, providing an energy resolution of 10000/401 eV (E/ ΔE). Images were recorded at selected energies through the Cr 2p region (570–585 eV) or Fe 2p region (700–715 eV). The photon energy was calibrated by measuring pure Cr or Fe in the experimental chamber.

3. Results

3.1. Weight loss and molten salt composition analysis

The weight loss of the Hastelloy N alloy specimens immersing in FLiNaK salts after 400 h is about 0.75 mg/cm^2 . Fig. 2 shows the average corrosion rates of the tested Hastelloy N alloy, comparing with other's work [7,10,18,25]. Obviously, the average corrosion rates of Hastelloy N alloy immersed in FLiNaK salts within 500 h are much larger than those tested for 1000 h. Among all of the corrosion work, FLiNaK salts with moisture [10] are of the most corrosion severity to the Hastelloy N alloys.

The chemistry change of FLiNaK salts after corrosion is shown in Table 2. The concentration of Fe decreased about 80% and those of Cr, Ni and Mo all increase about 50%. It indicates that Cr, Ni, Mo were depleted from the Hastelloy N alloy into the FLiNaK salts and Fe in the FLiNaK salts may diffuse into the alloy during the corrosion process.

3.2. Microstructural characterization

3.2.1. XRD analysis

The penetration depth of X-ray ($\lambda = 1.5406 \text{ \AA}$) for Hastelloy N alloy is evaluated about 11.3 μm . Fig. 3(a) shows the XRD patterns of Hastelloy N alloy surface before and after corrosion tests. In both

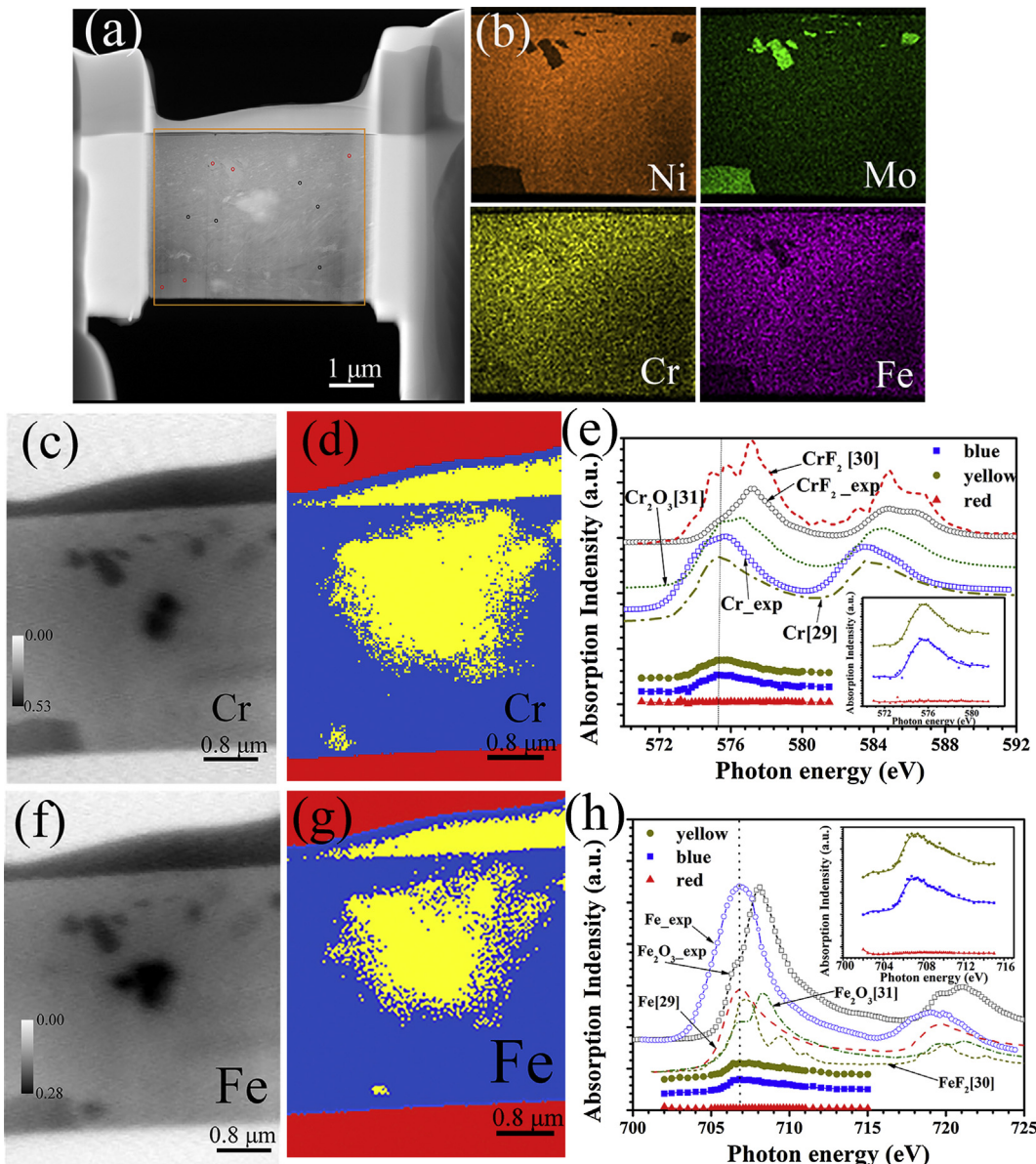


Fig. 6. (a): TEM images of as-received Hastelloy N alloy milled by FIB. The black and red circles show the matrix and carbide zones, respectively, for TEM/EDS point analysis; (b): TEM/EDS maps of rectangle area in panel (a); (c and f): STXM transmission images of Cr (c) at 572 eV and Fe (f) at 702 eV. Grey-color bar values are estimated from Cr and Fe absorption coefficients and XAS measurements; (d and g): color-coded maps of Cr and Fe, derived from STXM Cr and Fe L-edge stack analyses. (e and h): XAS extracted from the image sequences of Cr (d) and Fe (g). Some standard compounds are used as references. The vertical black dotted lines in panels (e) and (h) indicate the characteristic peaks of Cr and Fe metal. The insets in (e) and (h) was zoomed in, to present the characteristic peaks of the solid signs below in the (e) and (h). (For interpretation of the references to color in this figure legend, the reader is referred to the web version of this article.)

XRD patterns, the characteristic peaks of (1 1 1), (2 0 0) and (2 2 0) of γ phase nickel alloy with face-centered cubic (fcc) crystal structure were clearly detected. The characteristic peaks significantly shift to higher 2θ after experiencing 400 h corrosion in molten FLiNaK salts, which indicates a decrease in lattice parameters. The lattice parameters for pre- and post-corrosion Hastelloy N alloys were calculated from the (1 1 1), (2 0 0) and (2 2 0) peaks by applying the Nelson–Riley Function [26]. The intercept points on y-axis suggest that the lattice parameter on the alloy surface layer decreases from 359.07 to 357.53 pm (Fig. 3(b)). This indicates that some alloy elements were depleted from the alloy surface layer, leading to the decrease of lattice parameter.

3.2.2. SEM and EPMA analysis

Fig. 4 shows the SEM images of Hastelloy N alloy surface after corrosion. It is obvious that numerous pits, with size about 200 nm

in diameter, arrange in a spiral on the alloy surface (Fig. 4(a)). Since the specimens before corrosion were polished, there should be no pits on the alloy surface, which indicates that the alloy surface is corroded by FLiNaK salts and some elements are depleted from the alloy surface. As shown in Fig. 4(b), there are no visible pits or holes in the near surface area, which is markedly different from the morphology of the surface (Fig. 4(a)).

EPMA mapping performed on the cross-sectional images (Fig. 5(a)) of the alloy shows the relatively low concentration of Cr in the near-surface region for all the corrosion specimens (Fig. 5(d)), besides the slight reduction in the concentrations of Mo and Ni. The depletion of Cr occurred throughout the grains, which is obviously not uniform and in some region severer depletion of Cr takes place. It is of note that the concentration of Fe in the Cr-depletion region are higher than the bulk (Fig. 5(e)), which is reasonably speculated to be sourced from the FLiNaK salts, due to the reduction in the

concentration of Fe in the FLiNaK salts after corrosion. Additionally, many carbides are distributed in the matrix of Hastelloy N alloy, which are rich in Mo and lack of Ni and Cr, consistent with others' work [27,28].

To evaluate corrosion attack depth, the maximum and uniform thickness of Cr-depletion layer and Fe-rich layer were measured and labeled in EMPA mappings. The maximum Cr depletion distance ($26.7 \mu\text{m}$) is about three times larger than uniform ones in other grains ($7 \mu\text{m}$), using a cut-out criterion of about 80% of the Cr concentration of as-received Hastelloy N. In the same region, thickness of Cr-depletion layer is larger than that of the Fe-rich layer. The maximum Fe-rich layer distance ($21.0 \mu\text{m}$) is about five times larger than uniform ones in other grains ($3.7 \mu\text{m}$), using the cut-out criterion of about 125% of the Fe concentration of as-received Hastelloy N alloy.

3.2.3. TEM and STXM analysis

Fig. 6 shows the elemental distribution and chemical state of the Hastelloy N alloy before corrosion, characterized by TEM and SR-STXM. TEM/EDS maps shows that the main elements in the Hastelloy N alloy, Ni, Mo, Cr and Fe, are distributed uniformly in the matrix (**Fig. 6(b)**). **Fig. 6(e)** shows the Cr 2p soft X-ray absorption spectra (XAS) for the Hastelloy N alloy specimens before corrosion. They are compared with the XAS of Cr metal, CrF_2 and Cr_2O_3 , the former two both tested in this work and taken from Lopez's work [29] and Olalde-Velasco's work [30], and Cr_2O_3 [31] refers to Lopez's work. The XAS of Cr_2O_3 exhibits a peak at $\approx 576.5 \text{ eV}$ in the $2\text{p}_{3/2}$ region and a distinctive shoulder at $\approx 575 \text{ eV}$. The XAS of Cr metal has a different shape than that of Cr_2O_3 with a peak located at $\approx 575 \text{ eV}$. The Hastelloy N specimen before corrosion exhibits the typical XAS of Cr metal with a peak at 575 eV , suggesting that in this Hastelloy N alloy specimen almost no Cr oxides nor hydroxides are present in the near surface. Similarly, compared with the standard compound Fe [29], Fe_2O_3 [31] and FeF_2 [30], the Hastelloy N specimen before corrosion also exhibits the typical XAS of Fe metal with a peak located at $\approx 707 \text{ eV}$. The amplitude of XAS peaks can also be applied to characterize the concentration of the elements [32]. As shown in **Fig. 6(e)**, the amplitude of Cr XAS peaks of the blue area are almost equal to that of yellow area in **Fig. 6(d)**, meaning the concentration of Cr is almost uniform in the whole specimen. The concentration of Fe shows the similar uniform distribution.

As shown in **Fig. 7**, the cross section of the Hastelloy N alloy specimen after corrosion was milled into three parts by FIB: surface area ($0 \sim 5 \mu\text{m}$ away from the surface), middle area ($5 \sim 9 \mu\text{m}$ away from the surface) and bulk area ($9 \sim 13 \mu\text{m}$ away from the surface). **Fig. 8–10** show the elemental distribution and chemical state of the Hastelloy N alloy after corrosion, characterized by TEM and SR-STXM. As shown in **Fig. 8(e)**, there is no characteristic absorption peaks of Cr in the surface area ($0 \sim 5 \mu\text{m}$ away from the surface), which means the concentration of Cr is too low to be detected by the X-ray and severe depletion of Cr occurs in the near surface of Hastelloy N alloy. It is worth noting that the concentration of Fe in the blue area is higher than that of the yellow area closed to the bulk (**Fig. 8(g)**), which is also higher than the Fe concentration of the Hastelloy N alloy specimen before corrosion (**Fig. 8(h)**), and the Fe-rich layer is about $4 \mu\text{m}$, which is good accordance with the observation of Fe-rich layer by EPMA (**Fig. 5(e)**). The XAS peak of Fe in the surface area show no difference with those of the Fe metal and the Hastelloy N alloy, meaning no compounds with high valence state of Fe formed during the corrosion process. In addition, the TEM/EDS maps of the surface area show minor difference of the distribution of Cr and Fe, even the impurity stick to the surface of the specimen contaminated by the air (the yellow area in the center of **Fig. 8(d)** and red area in the center of **Fig. 8(g)**).

Fig. 9(e) shows the XAS of Cr in the middle area and it can be found that Cr exists in this area, and the concentration of Cr in this

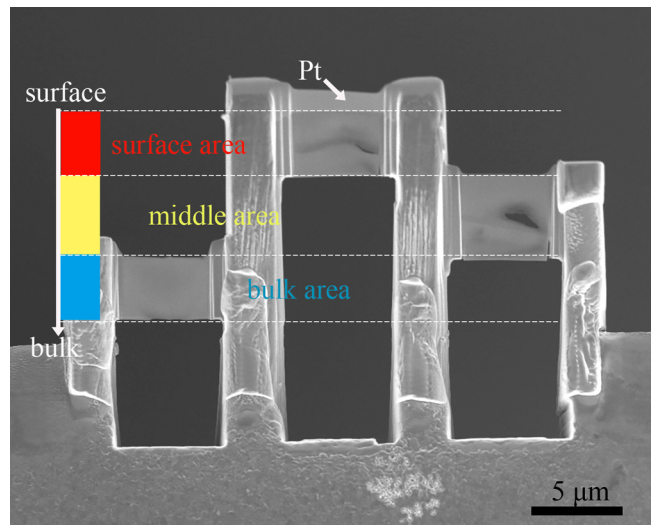


Fig. 7. FIB-SEM images of Hastelloy N alloy after corrosion testing in FLiNaK at 850°C for 400 h, milled by FIB. The specimen was divided into three part, surface area ($0 \sim 5 \mu\text{m}$ away from the surface), middle area ($5 \sim 9 \mu\text{m}$ away from the surface) and bulk area ($9 \sim 13 \mu\text{m}$ away from the surface).

area is much less than that of the specimen before corrosion. In addition, the XAS of Cr in the middle area show no difference with the Cr metal and the Hastelloy N alloy, pointing out that there is no new compound containing high valence state of Cr in the low-Cr area.

As shown in **Fig. 10(e)**, in the bulk area, the concentration of Cr in blue area (**Fig. 10(d)**) is closed to the specimens before corrosion, while some region (yellow area in **Fig. 10(d)**) is slightly lack of Cr (about 80% of the amplitude of the XAS peak of Cr in Hastelloy N alloy before corrosion). According to the Cr concentration distribution measured by SR-STXM, the thickness of the Cr-depletion layer is about $9 \mu\text{m}$, slightly larger than the evaluation value by EPMA.

In addition, it should be noted that carbides also change their chemistry during the corrosion process. As shown in **Fig. 6(a)**, carbides were distributed in the matrix of Hastelloy N alloy, which contains more Mo and less Ni, Cr than the matrix of Hastelloy N alloy. TEM analysis shows that the carbide possesses an fcc lattice and the estimated lattice parameter is about 1100 pm (**Fig. 11(a)**), which is coherent with matrix and determined as M_{12}C carbide [28]. The chemistry change of the carbides caused by corrosion were measured by TEM/EDS point analysis. The results, shown in **Fig. 11(b)**, reveal that the ratio of Ni, Mo and Cr atoms in M_{12}C carbides before corrosion is about 3:5:1. After corrosion in molten FLiNaK salts, the ratio of Ni, Mo and Cr atoms in M_{12}C changes to about 3:3:1. As shown in **Fig. 9(e)**, the Cr concentration of the M_{12}C carbide (yellow area in **Fig. 9(d)**) is slightly higher than the corroded Ni matrix (blue area), and the chemical state of Cr in the carbide does not change with the concentration, and still keeps zerovalent.

4. Discussion

As shown in **Fig. 2**, in both the present work and Olson's work [7], the Hastelloy N alloys were tested in FLiNaK salts at 850°C and the salts were purified to remove residual water. Though the concentration of metallic ions in the salts remained differences, the corrosion rates are very closed. In great contrast with the severely porous near-surface area observed by Olson et al. [7], there are no visible pits or holes in the near surface area (**Fig. 4(b)**), which in good accordance with the result that slightly less weight loss of our specimens than that measured by Olson. Both the corrosion rates in the present and Olson's work are about three order magnitude lower

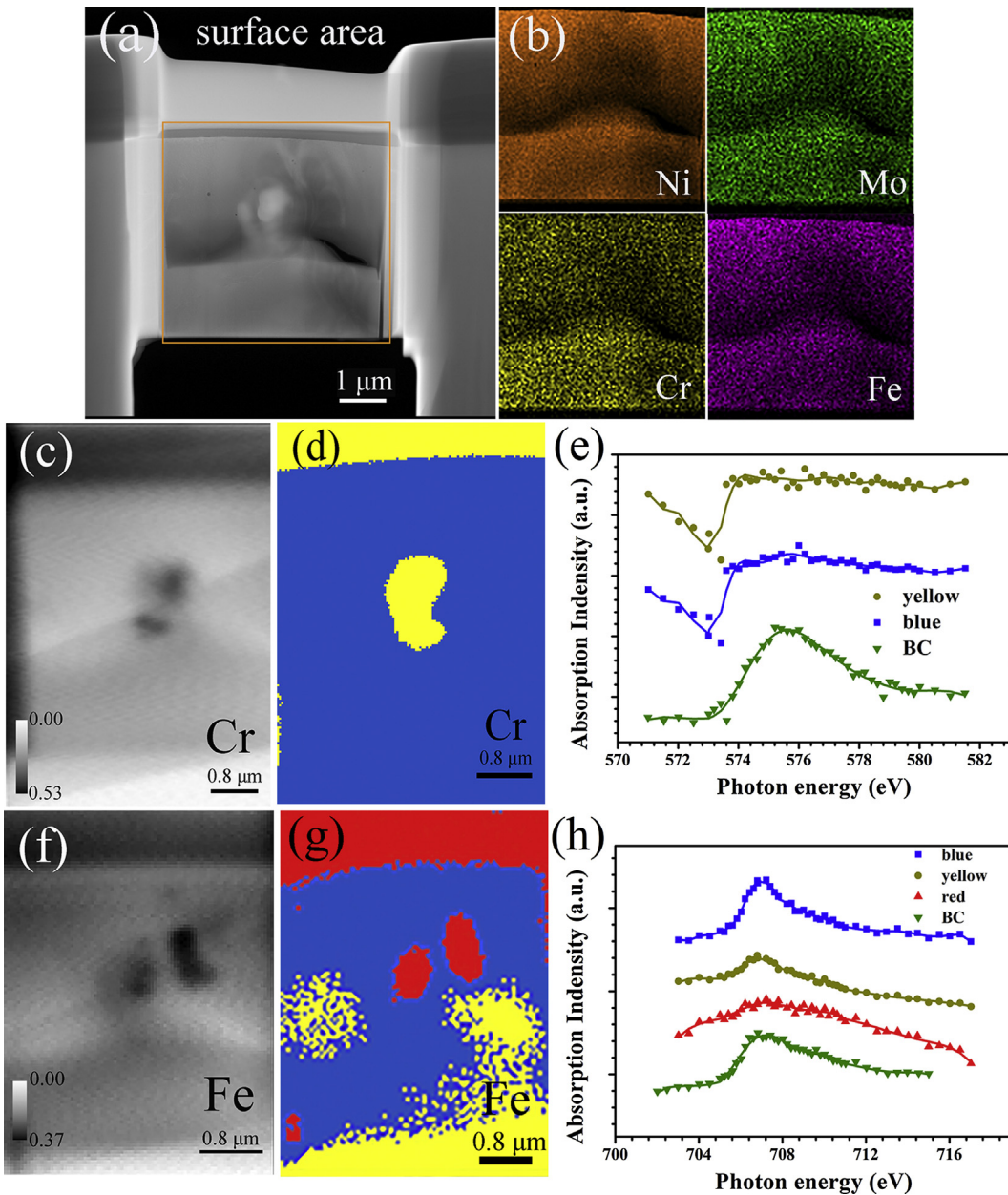


Fig. 8. (a): TEM images of the surface area ($0 \sim 5 \mu\text{m}$ away from the surface); (b): TEM/EDS maps of rectangle area in panel (a); (c and f): STXM transmission images of Cr (c) at 572 eV and Fe (f) at 702 eV; (d and g): color-coded maps of Cr and Fe, derived from STXM Cr and Fe L-edge stack analyses; (e and h): XAS extracted from the image sequences of Cr (c) and Fe (f), whose color stands for the same color area in panels (d) and (g). The green triangles in the (e) and (h) refer to Cr and Fe (blue solid square in Fig. 6(e)) and (h)) absorption intensity of Hastelloy N alloy before corrosion (BC). (For interpretation of the references to color in this figure legend, the reader is referred to the web version of this article.)

than that of corrosion in FLiNaK salts with moisture measured at 700°C by Ouyang et al. [10]. According to Arrhenius law, our corrosion reaction should be faster since the corrosion temperature is 150°C higher than that of Ouyang's. Therefore, it can be deduced that Fe and other metallic impurities are much less environmentally harmful substance than H_2O to the fluoride salts corrosion. In addition, the corrosion is expected to keep fast in the period of first 500 h because it is mainly accelerated by impurities, and then with the impurities tending to exhaust, intrinsic corrosion play dominant role and the corrosion is alleviated. Hence, the 1000 h corrosion tests [18,25] showed much slower average corrosion rates than ours.

In Hastelloy N alloy, Mo was considered as the most fluoride-resisted element in the alloy. Recently, Ouyang et al. [10,19]

reported the effect of Mo content on molten FLiNaK salts corrosion of Hastelloy N and Hastelloy B-3 alloys and found a depletion layer of Mo in the vicinity of the surface of the Hastelloy-B3 after 1000 h immersion, but not in the Hastelloy N alloy. In this work, it is found that the lattice parameter decreases from 359.07 to 357.53 pm by XRD analysis. The X-ray penetration depth for Hastelloy N alloy is about $11.3 \mu\text{m}$, which just covers the Cr-depletion layer. According to Vegard's law [33], the lattice parameter of Hastelloy N alloy can be calculated as,

$$a = 352.4 + 11.0X_{\text{Cr}} + 47.8X_{\text{Mo}} + 12.3X_{\text{Fe}} + 44.4X_{\text{W}} + 29.0X_{\text{Mn}} + 42.2X_{\text{Ti}} + 17.9X_{\text{Al}} \text{ (pm)} \quad (1)$$

where X_{Cr} , X_{Mo} , X_{Fe} , X_{W} , X_{Mn} , X_{Ti} and X_{Al} are the molar fraction of Cr, Mo, Fe, W, Mn, Ti and Al, respectively. The lattice parame-

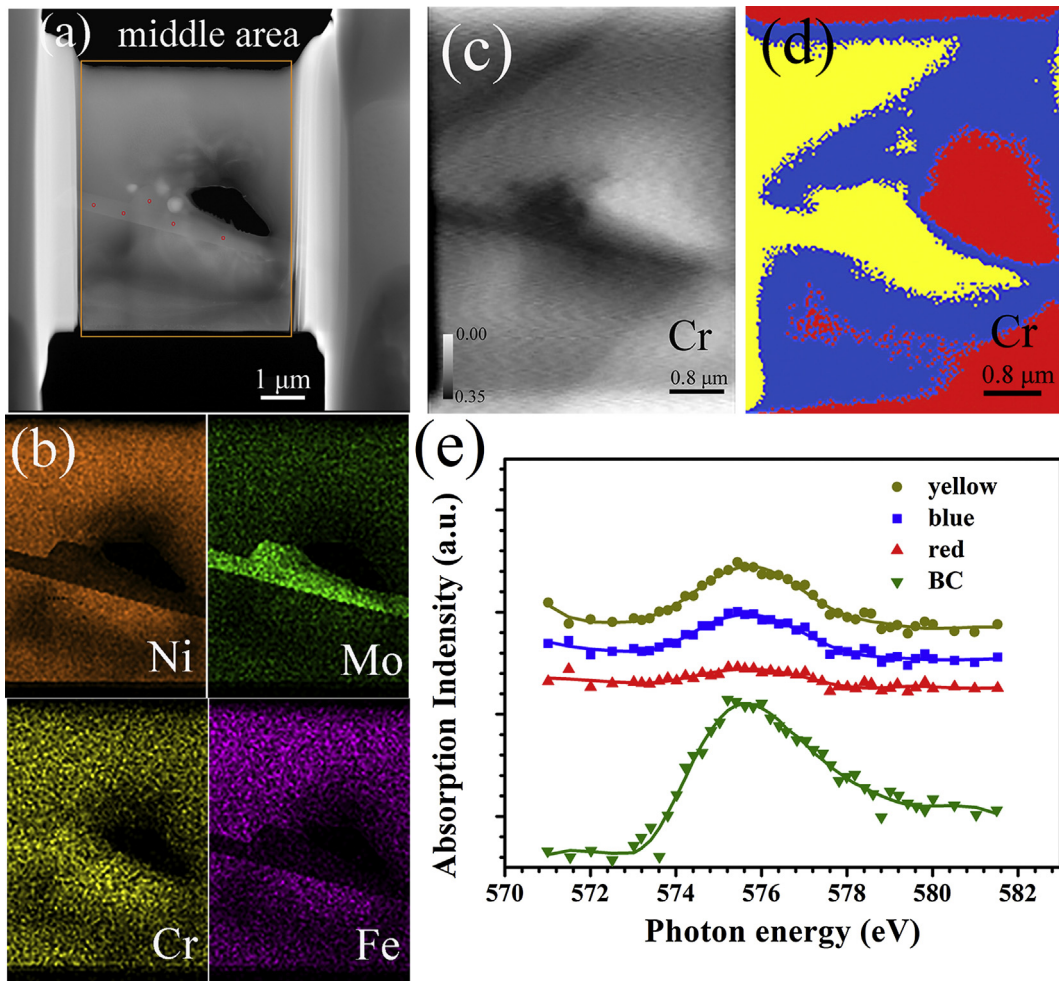
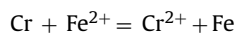
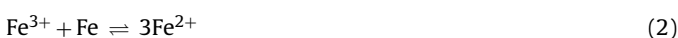


Fig. 9. (a): TEM images of the middle area ($5 \sim 9 \mu\text{m}$ away from the surface). The red circles show the carbide zones for TEM/EDS point analysis; (b): TEM/EDS maps of rectangle area in panel (a); (c): STXM transmission images of Cr at 572 eV; (d): color-coded maps of Cr, derived from an STXM Cr L-edge stack analysis; (e): XAS extracted from the image of Cr (c), whose color stands for the same color area in panel (d). The green triangles in the panel (e) refer to Cr (blue solid square in Fig. 6(e)) absorption intensity of Hastelloy N alloy before corrosion (BC). (For interpretation of the references to color in this figure legend, the reader is referred to the web version of this article.)

ter of the as-received Hastelloy N alloy is evaluated as 359.31 pm, which is only 0.06% larger than the evaluated value by XRD. The STXM analysis of Cr in the surface area (Fig. 8(e)) demonstrates that the Cr concentration on post-corrosion alloy surface is close to zero. Hence, the lattice parameter of the Hastelloy N alloy without Cr will decrease to 358.39 pm according to Eq. (1), which indicates that there should be other elements depleted from the alloy besides Cr. From the change of the compositions of FLiNaK salts before and after corrosion, it could be found in the main composition of Hastelloy N alloy, Ni, Mo and Cr were depleted from the alloy. Since the depletion of Ni and other minor element slightly affect the lattice parameter and the increase of Fe in the alloy can expand the lattice, it can be deduced that at least 20% of the whole Mo concentration was depleted from the Hastelloy N alloy during the corrosion process, to match the lattice parameter of 357.53 pm. Therefore, Mo depletion layer should exist in the surface of the Hastelloy N alloy, though EPMA and TEM/EDS did not detect it clearly.

Impurity-driven corrosion is believed to be the main harmful corrosion behavior occurred at a rapid rate in the initial stage of the corrosion process. It is known that the primary valence state of Cr and Fe in FLiNaK salts are Cr^{3+} and Fe^{3+} oxidation states [2]. In this work, the main impurity is Fe ion and it reacts with Cr in the alloy by [34,35]



In the molten FLiNaK salts, Fe^{3+} and Fe^{2+} keep equilibrium according to the Eq. (2) [35]. With the redox reaction between Fe^{2+} and Cr in the alloy surface, Fe^{3+} can also react with the Fe in the surface to maintain the equilibrium between Fe^{3+} and Fe^{2+} . Since the amount of Fe accumulating on the surface by Eq. (3) is more than that consumed by Fe^{3+} according to Eq. (2), Cr in the alloy surface can continuously react with Fe^{2+} and then a Cr-depletion and Fe-rich layer forms in the alloy surface until Fe^{3+} is exhausted. The STXM results show that the chemical states of Cr and Fe in the alloy surface area keep their zerovalent metal state. Fe atoms, accumulating on the surface, do not form any new compounds containing high valence state of Fe, which just diffuse into the bulk and fill in the voids caused by Cr depletion. It indicates that there is no other type of reaction, except the redox reaction Eq. (3), occurs between Fe ion and Cr during the corrosion process. Cr can be fluorinated immediately as it diffuses outwardly to the alloy surface, and the diffusion coefficient of Cr^{2+} ions in molten salt is approximately six orders of magnitude larger than that of Cr in the Ni matrix ($D_{\text{Cr}^{2+}/\text{FLiNaK}} = 2.9 \pm 0.8 \times 10^{-10} \text{ m}^2 \text{ s}^{-1}$ at 700°C) [36]. Therefore, the corrosion rate is mainly controlled by the diffusion of Cr outward to the alloy surface. The Cr-depletion layer is about 9 μm , while the Fe-rich layer is only about 4 μm , which indicates the diffusion rate of Cr is much faster than that of Fe in the Hastelloy N alloy. In fact,

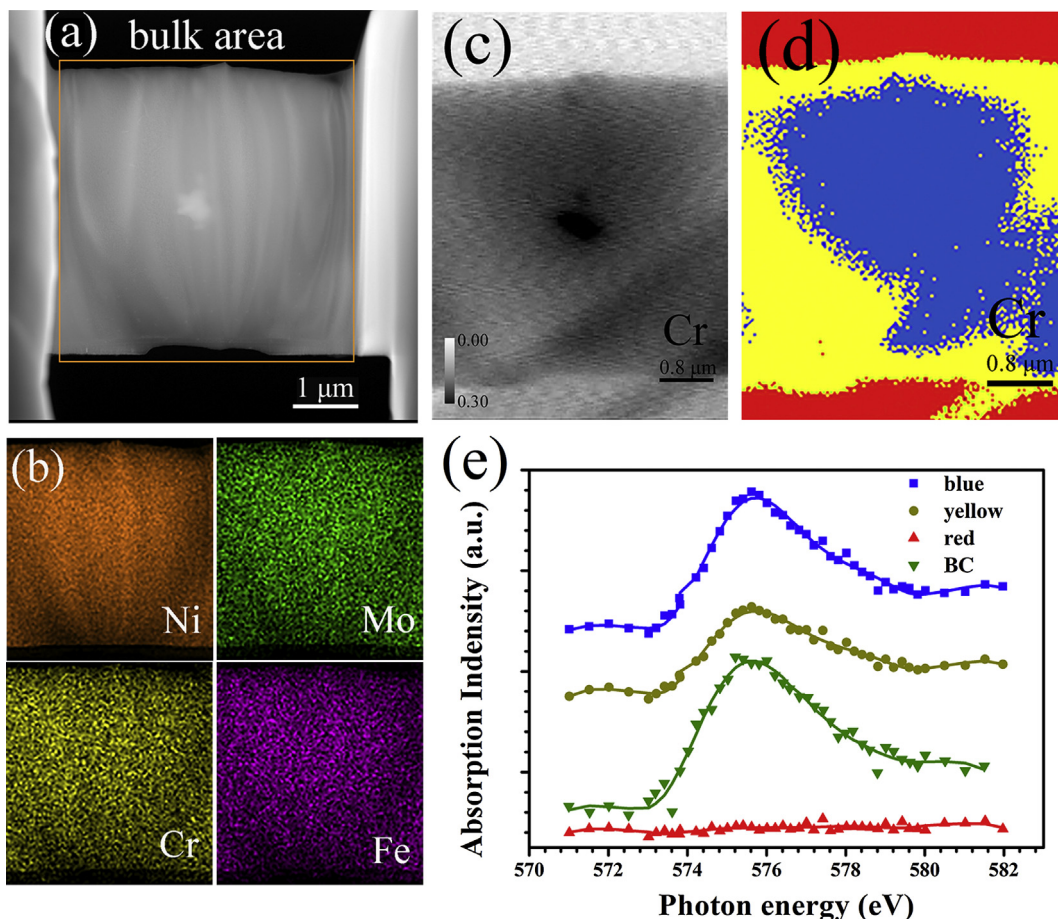


Fig. 10. (a): TEM images of the bulk area ($9 \sim 13 \mu\text{m}$ away from the surface); (b): TEM/EDS maps of rectangle area in panel (a); (c): STXM transmission images of Cr at 572 eV; (d): color-coded maps of Cr, derived from an STXM Cr L-edge stack analysis; (e): XAS extracted from the image of Cr (c), whose color stands for the same color area in panel (d). The green triangles in the panel (e) refer to Cr (blue solid square in Fig. 6(e)) absorption intensity of Hastelloy N alloy before corrosion (BC). (For interpretation of the references to color in this figure legend, the reader is referred to the web version of this article.)

the diffusion coefficient of Cr is much lower than that of Fe in Ni matrix without FLiNaK salts environment ($D_{\text{Cr}/\text{Ni}} = 1 \times 10^{-16} \text{ m}^2 \text{ s}^{-1}$ and $D_{\text{Fe}/\text{Ni}} = 4 \times 10^{-16} \text{ m}^2 \text{ s}^{-1}$ at 900°C) [37], which implies the Cr-concentration gradient between the surface and bulk greatly affecting the diffusion process. Since the Cr-concentration gradient is essentially caused by redox reaction between Fe ion impurity and Cr, it sounds plausible that the corrosion process is mainly controlled by the redox reaction between Fe ion and Cr. A characteristic diffusion distance can be conservatively estimated by [19]

$$x = \sqrt{2D_{\text{eff}}t} \quad (4)$$

where D_{eff} is overall effective diffusion coefficient and t is exposure time. The average diffusion coefficient of Cr in the grains is calculated as $2.81 \times 10^{-16} \text{ m}^2 \text{ s}^{-1}$, which is about 1/10 of that in the maximum Cr-depletion region ($2.48 \times 10^{-15} \text{ m}^2 \text{ s}^{-1}$); while the average diffusion coefficient of Fe in the grains is calculated as $5.56 \times 10^{-17} \text{ m}^2 \text{ s}^{-1}$, 1/30 of that in maximum Fe-rich region ($1.53 \times 10^{-15} \text{ m}^2 \text{ s}^{-1}$). Since Ni and Mo in the alloy are hard to react with the more active fluorides such as FeF_2 and CrF_2 , the depletion of Ni and Mo into the salt may be mainly caused by the trace amount of water in FLiNaK salts through the reaction:



where $\text{M} = \text{Ni}, \text{Mo}, \text{Cr}$. Additionally, the Cr concentration in the FLiNaK salts after corrosion should be beyond 100 ppm, according to the Eq. (3), but only about 40 ppm Cr were measured. The same thing happens to the Mo concentration. This may be caused by the Cr^{2+} and Mo^{2+} ions reacting with the graphite capsule to form carbides of Cr_3C_2 , Cr_7C_3 , and Mo_2C [18].

It should be noted that the M_{12}C carbide is greatly affected by the FLiNaK salts corrosion. The concentration of Cr in M_{12}C carbide before corrosion is slightly lower than that of the matrix (Figs. 6(b) and 11(b)). After corrosion, the concentration of Cr is obviously higher than that of the matrix, both of which are much lower than that of the matrix before corrosion (Fig. 9(d) and (e)). It suggests that Cr atoms in the M_{12}C carbide were depleted from the carbide during the corrosion process, and this depletion process is driven by the concentration gradient between the carbide and matrix. In other words, Cr atoms escape from the matrix into the molten salts, and made the concentration of Cr in M_{12}C carbide much higher than that of the matrix, further driving the transfer of Cr atoms from the carbide into the matrix. The Mo atoms in the carbide go through the similar process as Cr atoms and the ratio of Ni and Mo in the carbide change from 3:5 to about 1:1 (Fig. 11(b)).

5. Conclusions

(1) Cr and Mo are continuously depleted from the surface of Hastelloy N alloy into the molten FLiNaK salts at 850°C , while Fe ion

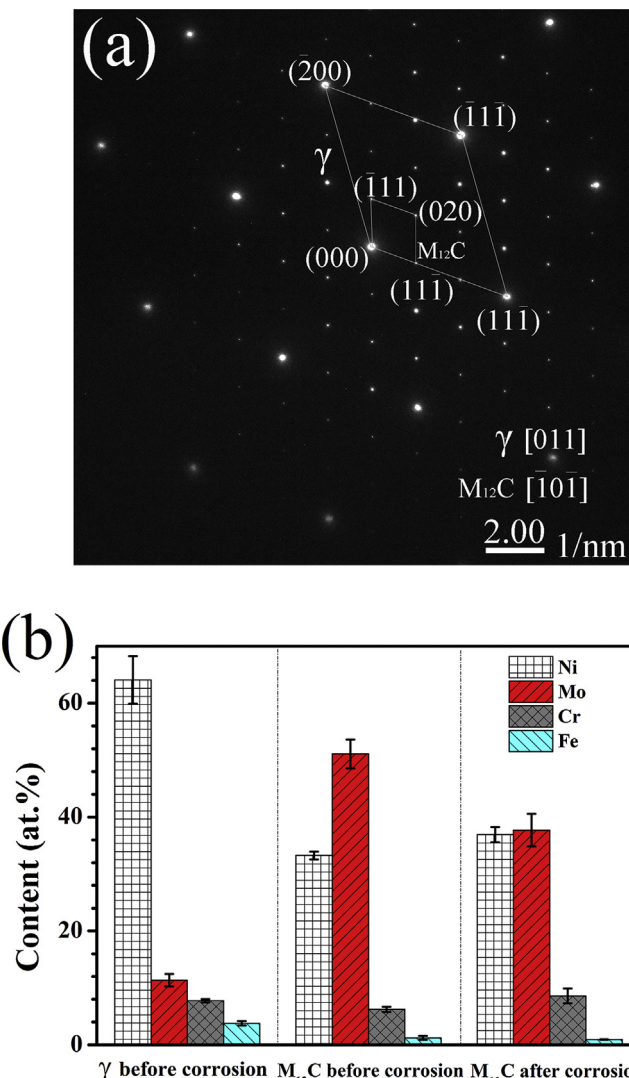


Fig. 11. (a) Selected area diffraction (SAD) pattern of orientation relationship between $M_{12}C$ carbide and matrix. (b) The chemistry of $M_{12}C$ carbide before and after corrosion in FLiNaK salts (at.%), measured by TEM/EDS point analysis. The zones measured are shown as circles in Figs. 6(a) and 9(a). The values are averaged over five data and error bars refer to the standard deviations.

- in the molten salts reacts with Cr, accumulating on the surface of the alloy, diffusing into the bulk and filling the voids that caused by Cr and Mo depletion.
- (2) The non-uniform corrosion of Hastelloy N alloy by molten FLiNaK salts was observed. The Cr-depletion layer is about $9.0 \mu\text{m}$ in the grains and about $26.7 \mu\text{m}$ in the maximum region, while the Fe-rich layer is about $4.0 \mu\text{m}$ in grains and $21.0 \mu\text{m}$ in the maximum region. The diffusion coefficient of Cr is higher than that of the Fe in the matrix of Hastelloy N alloy under the molten FLiNaK salts environment.
 - (3) In the molten FLiNaK salts with high Fe ions, the corrosion of Hastelloy N alloy was mainly controlled by the redox reaction between Fe ion and Cr. In the whole corrosion process, the Fe and Cr in the Hastelloy N alloy always keep zerovalent metal state, meaning no new compound with high valence state of Cr and Fe forms in the alloy surface.
 - (4) $M_{12}C$ carbide is greatly affected by the FLiNaK salts corrosion. The depletion of Cr and Mo also occurs in the carbides, driving by the concentration gradient between the carbide and the alloy matrix.

Acknowledgments

The authors deeply appreciate Drs. Xiangzhi Zhang, Junqin Li and Jiefeng Cao of Beamline BL08U1A at SSRF for their support of XAS and STXM. This work was supported by the Program of International S&T Cooperation, ANSTO-SINAP (Grant no. 2014DFG60230), the National Natural Science Foundation of China (Grant nos. 51371188 and 51501216), the Strategic Priority Research Program of the Chinese Academy of Sciences (Grant no. XDA02004210).

References

- [1] S. Delpech, C. Cabet, C. Slima, G.S. Picard, Mater. Today 13 (2010) 34–41.
- [2] D. Williams, L. Toth, K. Clarno, Assessment of candidate molten salt coolants for the advanced high temperature reactor (AHTR), in: ORNL/TM-2006/12, United States. Department of Energy (2006).
- [3] J. Serp, M. Allibert, O. Benes, S. Delpech, O. Feynberg, V. Ghetta, D. Heuer, D. Holcomb, V. Ignatiev, J.L. Kloosterman, L. Luzzi, E. Merle-Lucotte, J. Uhrl, R. Yoshioka, Z. Dai, Prog. Nucl. Energy 77 (2014) 308–319.
- [4] H. Bousier, S. Delpech, V. Ghetta, D. Heuer, D.-E. Holcomb, V. Ignatiev, E. Merle-Lucotte, J. Serp, The Molten Salt Reactor (MSR) in Generation IV: Overview and Perspectives, in: GIF Symposium Proceedings (2012) pp. 95.
- [5] W. Ren, G. Muralidharan, D.F. Wilson, D.E. Holcomb, Considerations of Alloy N for Fluoride Salt-Cooled High-Temperature Reactor Applications, in: Proceedings of the ASME Pressure Vessels and Piping Conference (2011) 57029.
- [6] H. Zhu, R. Holmes, T. Hanley, J. Davis, K. Short, L. Edwards, Corros. Sci. 91 (2015) 1–6.
- [7] L.C. Olson, J.W. Ambrosek, K. Sridharan, M.H. Anderson, T.R. Allen, J. Fluor. Chem. 130 (2009) 67–73.
- [8] H.E. McCoy, Oak ridge, Nat. Lab. Rev. 3 (1969) 35–48.
- [9] P. Calderoni, C. Cabet, Corrosion issues in molten salt reactor (MSR) systems, in: D. Féron (Ed.), Nuclear Corrosion Science and Engineering, Woodhead Publishing, 2012, pp. 842–865.
- [10] F.-Y. Ouyang, C.-H. Chang, B.-C. You, T.-K. Yeh, J.-J. Kai, J. Nucl. Mater. 437 (2013) 201–207.
- [11] M. Kondo, T. Nagasaka, T. Muroga, A. Sagara, N. Noda, Q. Xu, D. Ninomiya, N. Masaru, A. Suzuki, T. Terai, Fusion Sci. Technol. 56 (2009) 190–194.
- [12] M. Kondo, T. Nagasaka, V. Tsisar, A. Sagara, T. Muroga, T. Watanabe, T. Oshima, Y. Yokoyama, H. Miyamoto, E. Nakamura, N. Fujii, Fusion Eng. Des. 85 (2010) 1430–1436.
- [13] J.R. Keiser, Compatibility Studies of Potential Molten-Salt Breeder Reactor Materials in Molten Fluoride Salts, in: ORNL/TM-5783, Oak Ridge National Laboratory (1977).
- [14] J.W. Koger, Corrosion 29 (1973) 115–122.
- [15] Y. Wang, H. Liu, C. Zeng, J. Fluor. Chem. 165 (2014) 1–6.
- [16] D. Olander, J. Nucl. Mater. 300 (2002) 270–272.
- [17] D. Ingersoll, C. Forsberg, P. MacDonald, ORNL/TM-2006/140, Oak Ridge National Laboratory (2007).
- [18] R.S. Sellers, W.-J. Cheng, B.C. Kelleher, M.H. Anderson, K. Sridharan, C.-J. Wang, T.R. Allen, Nucl. Technol. 188 (2014) 192–199.
- [19] F.-Y. Ouyang, C.-H. Chang, J.-J. Kai, J. Nucl. Mater. 446 (2014) 81–89.
- [20] C. Peng, B.W. Jiang, Q. Liu, Z. Guo, Z.J. Xu, Q. Huang, H.J. Xu, R.Z. Tai, C.H. Fan, Energy Environ. Sci. 4 (2011) 2035–2040.
- [21] L. Salvo, P. Cloetens, E. Maire, S. Zabler, J.J. Blandin, J.Y. Buffière, W. Ludwig, E. Boller, D. Bellet, C. Josserand, Nucl. Instrum. Methods B 200 (2003) 273–286.
- [22] Y. Leon, M. Saheb, E. Drouet, D. Neff, E. Foy, E. Leroy, J.J. Dynes, P. Dillmann, Corros. Sci. 88 (2014) 23–35.
- [23] A. Michelin, E. Burger, E. Leroy, E. Foy, D. Neff, K. Benzerara, P. Dillmann, S. Gin, Corros. Sci. 76 (2013) 403–414.
- [24] C. Xue, Y. Wang, Z. Guo, Y. Wu, X. Zhen, M. Chen, J. Chen, S. Xue, Z. Peng, Q. Lu, R. Tai, Rev. Sci. Instrum. 81 (2010) 103502.
- [25] D.E. Holcomb, G. Muralidharan, D.F. Wilson, Creep-Resistant, Cobalt-Free Alloys for High Temperature, Liquid-Salt Heat Exchanger Systems, United States Patent Publication, US 2015/0044088 A1.
- [26] J.B. Nelson, D.P. Riley, Proc. Phys. Soc. 57 (1945) 160.
- [27] Z.F. Xu, L. Jiang, J.S. Dong, Z.J. Li, X.T. Zhou, J. Alloys Compd. 620 (2015) 197–203.
- [28] T. Liu, J.S. Dong, L. Wang, Z.J. Li, X.T. Zhou, L.H. Lou, J. Zhang, J. Mater. Sci. Technol. 31 (2015) 269–279.
- [29] M.F. López, A. Gutiérrez, F.J. Pérez, M.P. Hierro, F. Pedraza, Corros. Sci. 45 (2003) 2043–2053.
- [30] P. Olalde-Velasco, J. Jimenez-Mier, J. Denlinger, W.L. Yang, Phys. Rev. B 87 (2013) 245136.
- [31] J.M. Bastidas, M.F. López, A. Gutiérrez, C.L. Torres, Corros. Sci. 40 (1998) 431–438.
- [32] P. Zhang, Y.H. Ma, Z.Y. Zhang, X. He, J. Zhang, Z. Guo, R.Z. Tai, Y.L. Zhao, Z.F. Chai, ACS Nano 6 (2012) 9943–9950.
- [33] R.C. Reed, The Superalloys: Fundamentals and Applications, Cambridge University Press, 2006.

- [34] K. Sridharan, T.R. Allen, Corrosion in molten salts, in: F.L. Groult (Ed.), *Molten Salts Chemistry*, Elsevier, Oxford, 2013, pp. 241–267.
- [35] J. Redman, Effect of Fuel Composition on the Equilibria $3\text{CrF}_2=2\text{CrF}_3+\text{Cr}^\circ$ and $3\text{FeF}_2=2\text{FeF}_3+\text{Fe}^\circ$, in: H.G. MacPherson, Molten Salt Reactor Quarterly Progress Report, ORNL-2626 (1959) 95–96.
- [36] H.O. Nam, A. Bengtson, K. Vörtler, S. Saha, R. Sakidja, D. Morgan, *J. Nucl. Mater.* 449 (2014) 148–157.
- [37] R.C. Reed, T. Tao, N. Warnken, *Acta Mater.* 57 (2009) 5898–5913.